Oxygen Bridges between NiO Nanosheets and Graphene for Improvement of Lithium Storage

Guangmin Zhou,[†] Da-Wei Wang,[‡] Li-Chang Yin,[†] Na Li,[†] Feng Li,[†,*] and Hui-Ming Cheng[†]

[†]Shenyang National Laboratory for Materials Science, Institute of Metal Research, Chinese Academy of Sciences, 72 Wenhua Road, Shenyang 110016, China, and [‡]ARC Centre of Excellence for Functional Nanomaterials, Australian Institute for Bioengineering and Nanotechnology, The University of Queensland, Brisbane, Qld 4072, Australia

ABSTRACT

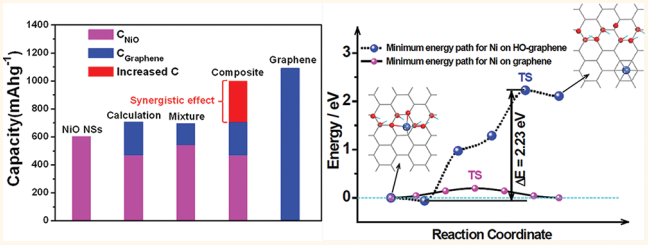

Graphene has been widely used to dramatically improve the capacity, rate capability, and cycling performance of nearly any electrode material for batteries. However, the binding between graphene and these electrode materials has not been clearly elucidated. Here we report oxygen bridges between graphene with oxygen functional groups and NiO from analysis by X-ray photoelectron spectroscopy, Fourier transform infrared spectroscopy, and Raman spectroscopy and confirm the conformation of oxygen bridges by the first-principles calculations. We found that NiO nanosheets (NiO NSs) are bonded strongly to graphene through oxygen bridges. The oxygen bridges mainly originate from the pinning of hydroxyl/epoxy groups from graphene on the Ni atoms of NiO NSs. The calculated adsorption energies (1.37 and 1.84 eV for graphene with hydroxyl and epoxy) of a Ni adatom on oxygenated graphene by binding with oxygen are comparable with that on graphene (1.26 eV). However, the calculated diffusion barriers of the Ni adatom on the oxygenated graphene surface (2.23 and 1.69 eV for graphene with hydroxyl and epoxy) are much larger than that on the graphene (0.19 eV). Therefore, the NiO NS is anchored strongly on the graphene through a C—O—Ni bridge, which allows a high reversible capacity and excellent rate performance. The easy binding/difficult dissociating characteristic of Ni adatoms on the oxygenated graphene facilitates fast electron hopping from graphene to NiO and thus the reversible lithiation and delithiation of NiO. We believe that the understanding of this oxygen bridge between graphene and NiO will lead to the development of other high-performance electrode materials.

KEYWORDS: graphene · NiO nanosheets · oxygen bridge · oxygen functional groups · density functional theory · lithium ion batteries

Metal oxides have evolved as an important family of anode materials to be a high-capacity alternative to graphite.[1] They also have a safe lithiation potential that isolates the problematic lithium plating process.[2] However, the use of metal oxides for lithium ion batteries (LIBs) has been limited mainly by their low electrical conductivity, easy agglomeration, and inferior cycling stability resulting from a large volume change during lithiation/delithiation. To circumvent these challenges, uses of good conductive matrix and nanostructured metal oxides and their composites with carbonaceous materials are the efficient methods to improve the cycling stability of metal oxides by suppressing their volume change and increasing their electrical conductivity.[3−8]

Graphene with intrinsically excellent electrical conductivity and mechanical flexibility is proposed as one of the most appealing carbon materials for this purpose.[9−11] A variety of metal oxides with different sizes and morphologies have been blended with graphene as anode materials for LIBs and have improved the capacity, rate capability, and cycling stability.[10,12−19] Many reports have ascribed the phenomenon to "synergistic effects" resulting from their good "interfacial interaction", which induces better performance than each individual component and the total sum of the individual effects.[12,13,16−18,20] However, the terms "synergistic effect" and "interfacial interaction" are too vague to indicate the exact interaction mechanism. Therefore, research to clarify the details, both experimentally and theoretically, is important and urgent. It is noted that metal oxides can be better dispersed on higher oxygen content, or oxygen-rich graphene, which suggests a unique role of oxygen functional groups in increasing the interfacial interaction in graphene/metal oxide systems.[20−23]

Graphene is a sheet, and we consider that a sheet-on-sheet (metal oxide/graphene) nanostructure is beneficial for ions and electrons to access their surface, consequently enabling a fast conversion reaction. More importantly, due to the larger contact interface and more linkage sites, a sheet-like

* Address correspondence to fli@imr.ac.cn.

Received for review January 9, 2012 and accepted March 18, 2012.

Published online March 18, 2012
10.1021/nn300098m

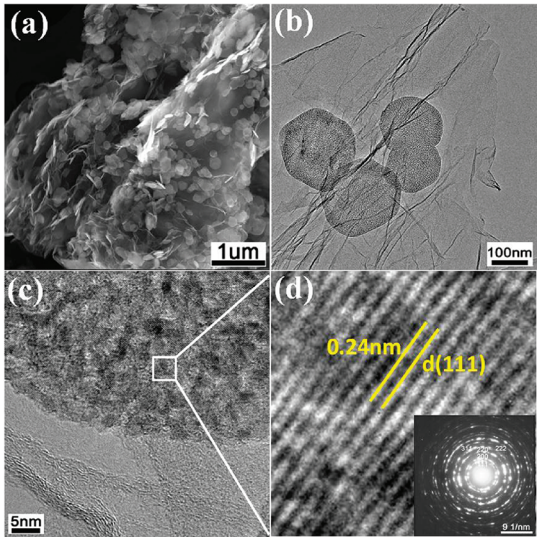

Figure 1. (a) SEM image of the NiO NS/graphene composite, (b) TEM and (c) HRTEM images of the NiO NS/graphene composite, (d) enlarged image of the square area in (c), and inset is the SAED pattern of the NiO NS/graphene composite.

structure is more desirable to investigate the interaction between metal oxide and graphene than a spherical particle-like morphology. Two-dimensional (2D) NiO nanosheets (NiO NSs) have a similar structure to graphene and can be used as a model material for constructing a layered nanostructure, which has shown potential for use in LIBs.[18,24,25]

Herein, we grow NiO NSs on graphene and explore the interaction between NiO and graphene. Combining the experimental results and the first-principles calculations, we elucidate the existence of oxygen bridges between NiO and graphene, which can improve the cyclic stability and high rate capability. We propose that the oxygen bridges between nickel oxide (probably many other metal oxides) and graphene-containing oxygen functional groups are the origin of the synergistic effect and interfacial interaction.

RESULTS AND DISCUSSION

Scanning electron microscopy (SEM) and transmission electron microscopy (TEM) images show that the NiO NS/graphene multilayer structure obtained is composed of sheet-like NiO homogeneously grown on graphene, forming a 2D sheet-on-sheet structure (Figure 1a,b). The size of the NiO NSs ranges from 100 to 200 nm. The presence of NiO NSs between graphene effectively prevents the agglomeration and restacking of graphene and consequently helps maintain their high active surface area, which is favorable for increasing accessible reaction sites. It can be seen that NiO NSs are firmly anchored on graphene even after ultrasonic dispersion for TEM characterization (Figure S1 in the Supporting Information), indicating a strong linkage between them. The surface functional groups of graphene provide preferred nucleation sites for the growth of NiO, thus enabling a good dispersion of NiO NSs on the graphene support.[21] In comparison, the NiO NSs obtained from the same experimental condition but without graphene tend to form an agglomerated structure, as shown in Figure S2a,b. From the cross-sectional TEM images, the thickness of the NiO NSs is estimated to be 30−50 nm (Figure S2b). As for a NiO NS−graphene mixture (prepared by grinding the same amount of graphene and NiO NSs as found in the NiO NS/graphene composite), the NiO NSs are sparsely distributed on the surface of graphene through weak van der Waals forces (Figure S3). Figure 1c shows a high-resolution TEM (HRTEM) image of the NiO NS/graphene composite taken from an edge, from which we can clearly see the periodic fringes of graphene and NiO NSs. The enlarged image of the square area in panel c, as shown in Figure 1d, reveals lattice fringes with an interplanar spacing of 0.24 nm corresponding to the (111) lattice planes of cubic NiO. The rings (inset of Figure 1d) obtained in the selected area electron diffraction (SAED) patterns reveal that the NSs attached to the graphene were crystalline NiO.

Due to the 2D sheet-on-sheet structure with less agglomeration for NiO NSs and graphene, we expect a higher contact surface area with more linkage sites in the multilayer structure. The differences in Brunauer−Emmett−Teller (BET) specific surface area and porous structure between the NiO NS/graphene composite, NiO NS−graphene mixture, and NiO NSs were investigated by nitrogen adsorption. The BET specific surface area and pore volume are 188 $m^2 g^{-1}$ and 0.26 $cm^3 g^{-1}$ for the NiO NS/graphene composite, higher than those of the NiO NS−graphene mixture (132 $m^2 g^{-1}$, 0.24 $cm^3 g^{-1}$) and NiO NSs (89 $m^2 g^{-1}$, 0.06 $cm^3 g^{-1}$). The weight percentage of graphene in the composite is 21.8 wt %, determined by thermogravimetric analysis (TGA) as shown in Figure S4. Accordingly, the BET specific surface area of the composite is also larger than the simple sum ($89 \times 78.2\% + 376 \times 21.8\% = 152$ $m^2 g^{-1}$) based on the rule of mixtures from individual graphene (376 $m^2 g^{-1}$) and NiO NSs. These results can be ascribed to the NiO NSs on the surface and between graphene layers, which prevent the graphene from aggregating and restacking after the removal of solvents. Thus the high specific surface area and pore volume of the composite were maintained.

The binding between the graphene and NiO NSs was studied by X-ray photoelectron spectroscopy (XPS), which revealed the presence of carbon, oxygen, and nickel (Figure 2a). A Gaussian fit to the C 1s spectrum of graphene and the NiO NS/graphene composite shows three different peaks at 284.6, 285.7, and 289.4 eV, corresponding to nonoxygenated carbon atoms (C−C/C═C), carbon atoms in hydroxyl groups (C−OH/C−ONi), and carbon in carboxyl groups (HO-C═O), respectively (Figure S5).[26] Hydroxyl groups show a

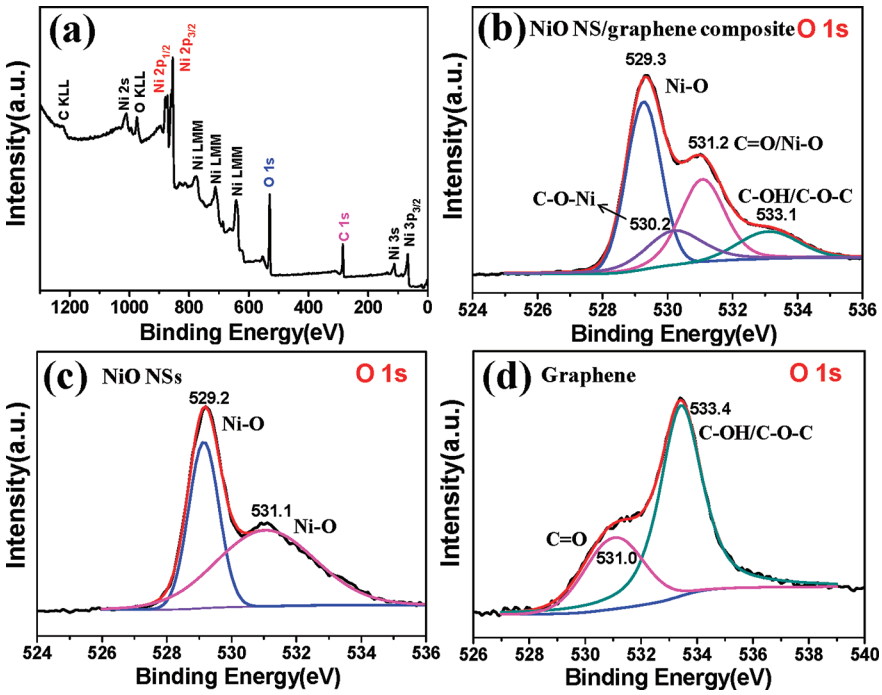

Figure 2. (a) XPS spectrum of the NiO NS/graphene composite. (b) O 1s XPS spectrum of the NiO NS/graphene composite. (c) O 1s XPS spectrum of the NiO NSs. (d) O 1s XPS spectrum of the graphene.

much higher intensity than do carboxyl groups. In the spectra of Ni 2p (Figure S6), the peaks centered at 851−865 and 870−885 eV with a main peak and satellite peak are attributed to the Ni $2p_{3/2}$ and Ni $2p_{1/2}$ spin−orbit levels of NiO.[25] Figure 2b shows the O 1s XPS spectrum of the NiO NS/graphene composite, which can be deconvoluted into four peaks. The peak at 529.3 eV corresponds to oxygen in NiO,[25,27] consistent with the O 1s spectrum of the NiO NSs (Figure 2c). The peak at 531.2 eV is assigned to C═O groups or shoulder peak of O 1s in NiO, and the peak at 533.1 eV is ascribed to C−OH and/or C−O−C groups (hydroxyl and/or epoxy).[28,29] Moreover, compared with the peak located at 533.4 eV in O 1s spectrum of the pristine graphene (Figure 2d), the content of C−OH and/or C−O−C groups in the composite (Figure 2b) is dramatically smaller, which suggests the replacement of hydrogen in hydroxyl groups or a possible ring-opening reaction of epoxy groups[30] by Ni^{2+} in NiO forming the C−O−Ni linkage. The extra peak located at 530.2 eV is attributed to the possible formation of a Ni−O−C bond. The binding of Ni^{2+} with graphene might be either with carbon atoms or with oxygen-containing functional groups on the surface of graphene. However, the first possibility is excluded as the contribution from C or Ni atoms in the C−Ni bond is absent at 283.5 eV in the C 1s spectrum (Figure S5b) or at 853.5 eV in the Ni $2p_{3/2}$ spectrum[31] (Figure S6). As a result, we believe that NiO anchors on the oxygenated graphene through a C−O−Ni linkage.

The C−O−Ni linkage between graphene and NiO demonstrated in XPS was further corroborated by Fourier transform infrared spectroscopy (FTIR). The structure of the graphene, NiO NS/graphene composite, residual graphene after dissolving NiO NSs in HCl from the composite, and NiO NSs was analyzed by FTIR in the 1800−400 cm^{-1} spectral region, as shown in Figure 3. The absorption band at 1635 cm^{-1} for these samples is assigned to the bending vibration of O−H (adsorbed water molecules).[32,33] The FTIR spectra of the NiO NS/graphene composite and NiO NSs show peaks at 415 and 563 cm^{-1} that are derived from the stretching vibration of NiO.[34] The characteristic peaks for graphene at 1421, 1162, and 1025 cm^{-1} are, respectively, due to O−H deformation vibration, C−O vibration of the C−OH, and C−O−C vibration of the epoxy.[33,35,36] However, after the growth of NiO NSs, the intensity of the C−OH band at 1162 cm^{-1} significantly decreases and the peaks corresponding to the O−H and C−O−C groups at 1421 and 1025 cm^{-1} are even absent (denoted by a pink rectangle). Furthermore, after removing the NiO NSs by reaction with HCl, the oxygen functional groups are recovered (as marked by black arrows). This result suggests that the epoxy and hydroxyl groups are broken down to form a C−O−Ni linkage between graphene and NiO, but the NiO removal restores these oxygen-containing groups.

Raman spectra of the samples are shown in Figure 4a. There are two prominent peaks at 1330 and 1594 cm^{-1} for the NiO NS/graphene composite, which correspond to the D and G bands of graphene.[37] The G band shift in carbon-based composites relates to the charge transfer between the carbon and other compounds present.[38−40] Therefore, the observed shift by 11 cm^{-1}

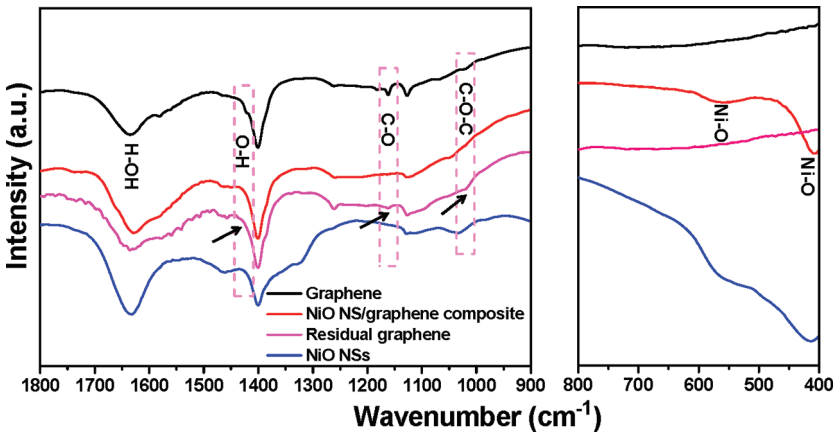

Figure 3. FTIR spectra of the graphene, NiO NS/graphene composite, residual graphene after dissolving NiO NSs from the composite, and NiO NSs.

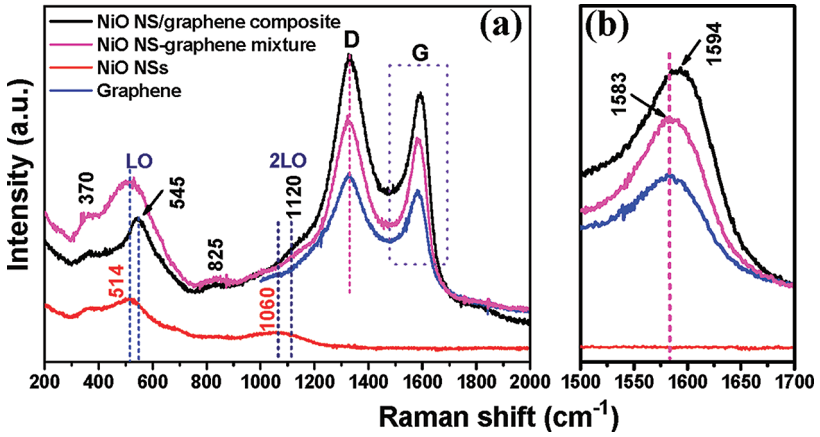

Figure 4. (a) Raman spectra of the NiO NS/graphene composite, NiO NS−graphene mixture, NiO NSs, and graphene. (b) Enlarged G band of the NiO NS/graphene composite, NiO NS−graphene mixture, and graphene marked by a rectangle in (a).

from 1583 (graphene) to 1594 cm^{-1} (NiO NS/graphene composite) indicates the presence of a charge transfer from graphene to NiO NSs (Figure 4b). The G band of the NiO NS−graphene mixture located at the same position as that of graphene suggests a weak interaction between graphene and NiO NSs in the mixture. Besides the two peaks, there are four Raman peaks located at 370, 545, 825, and 1120 cm^{-1}, which could be assigned to the first-order transverse optical (TO), longitudinal optical (LO), 2TO, and 2LO phonon modes of NiO, respectively.[41] The peaks of the NiO NSs, NiO NS−graphene mixture, and NiO NS/graphene composite at 370 and 825 cm^{-1} are in the same positions, while the LO and 2LO phonon modes of the NiO NS/graphene composite shift to a higher frequency. The Raman shift in the NiO NS/graphene composite could be induced by the doping effect and/or bonding formation, whereas the same positions of G band as graphene and LO, TO modes as NiO NSs in NiO NS−graphene mixture indicate the absence of (or negligible contribution from) doping effect. Therefore, the shift of G band and LO modes also suggests bond formation between graphene and NiO NSs.

To better understand the C−O−Ni linkage between graphene and NiO, we performed density functional theory (DFT) calculations to explore the nature of the binding of nickel on the surface of graphene with oxygen-containing functional groups. On the basis of the present experimental results, the residual oxygen-containing functional groups on the graphene are mainly hydroxyl and epoxy, which is well understood by a recent theoretical prediction.[42] We consider an isolated Ni atom approaching the surface of a graphene with hydroxyl (HO-graphene) or epoxy groups (EO-graphene) as the first step for growing NiO NSs on the graphene surface. The detachment from, and further diffusion on, the HO-graphene/EO-graphene was investigated to explore the interaction between HO-graphene/EO-graphene and NiO. We also studied a similar diffusion process for an isolated Ni adatom on a graphene surface for comparison. First-principles calculations were performed to investigate the energetics and dynamics for these processes. Three possible adsorption sites for an isolated Ni adatom on a graphene surface are considered, as shown in Figure S7a. On the basis of our calculations, a hollow site is the

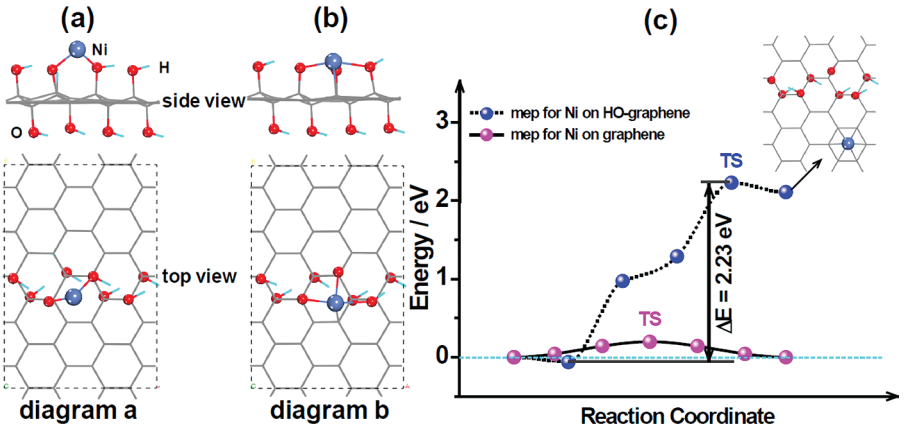

Figure 5. Local minimum adsorption states: (a) diagram a and (b) diagram b of a Ni atom binding with HO-graphene, and (c) the minimum energy path (mep) for a Ni adatom diffusing on the graphene and HO-graphene surface.

most energetically favorable site for an isolated Ni adatom on the graphene with an adsorption energy, 1.26 eV, which is much lower than the cohesive energy (4.44 eV/atom) of bulk Ni.[43] It should be noted that our result is in good agreement with previous first-principles calculations.[44−46] By using the climbing nudged elastic band (cNEB) method, the energy barrier for an isolated Ni adatom to diffuse from a hollow site to a neighboring hollow site on graphene was calculated to be 0.19 eV, indicating that an isolated Ni adatom easily diffuses and prefers to cluster on the graphene surface. In the case of HO-graphene, two local minimum adsorption states are observed after full relaxation when an isolated Ni atom approaches the hydroxyl groups on the HO-graphene surface from a distant (8 Å from the HO-graphene surface) out-of-plane position. The first (diagram a) is where the Ni adatom bonds with two O atoms and pushes aside one H atom to the surface forming a C−H bond (Figure 5a), the second (diagram b) is where the Ni adatom bonds with three O atoms after crowding out two H atoms to form a H_2 molecule, as shown in Figure 5b. It should be noted that a similar deprotonation process was observed in organometallic Ti fragments grafted onto mesoporous silica.[47] The adsorption energies for these two adsorption states were calculated to be 1.22 (diagram a) and 1.37 eV (diagram b). In the case of EO-graphene, ring opening occurs for two adjacent in-plane epoxy groups when a Ni atom approaches toward the EO-graphene surface (inset of Figure S8), resulting a calculated adsorption energy, 1.84 eV, for a Ni adatom bonding with two oxygen atoms. These adsorption energies for a Ni adatom on the oxygenated graphene surface are comparable with that (1.26 eV) on graphene. Therefore, besides the binding energy, we speculate that the detachment of the bonded Ni atom from oxygen atoms and its further diffusion on the HO-graphene/EO-graphene surface should be different from that on a graphene surface. Here, we choose diagram b as the reactant and study the dynamics of the Ni adatom detaching from the oxygen atom and diffusing on the HO-graphene surface. As expected, the energy barrier was calculated to be 2.23 eV (Figure 5c), which is more than 10-fold that on the graphene (0.19 eV). As for Ni adatom on EO-graphene surface, the energy barrier was calculated to be 1.69 eV (Figure S8). These very large energy barriers (2.23 and 1.69 eV for HO-graphene and EO-graphene, respectively) indicate that it is hard to detach from the oxygenated graphene for the bonded Ni adatom. Because of the linkage between Ni and O atoms, we expect a large electron charge overlap in the interface between the NiO NSs and graphene, providing a good pathway for electron transport during charge/discharge cycles. On the basis of our first-principles calculations, the residual hydroxyl/epoxy groups on the graphene show a strong pinning effect on the Ni atoms of the NiO NSs (hereafter the C−O−Ni linkage referred to an oxygen bridge), which is expected to play an important role in improving the electrochemical performance of the NiO NS/graphene composite.

To determine whether the functionality of oxygen bridges between graphene and NiO could improve the NiO NS/graphene anode performance, a galvanostatic charge−discharge cycling test was carried out. Figure 6a−c shows the first, fifth, 10th, and 20th discharge−charge voltage profiles of the NiO NS/graphene composite, NiO NS−graphene mixture, and NiO NSs at a constant current of 50 mA g^{-1}. In the first discharge curve, an extended voltage plateau was found around 0.75 V for the three samples, which is ascribed to the formation of a solid electrolyte interface (SEI) film and the reduction of Ni^{2+} to Ni^0 according to $2Li + NiO \rightarrow Li_2O + Ni$.[1,25] In addition, a more inclined discharge slope between 0.75 and 0.001 V is present for the NiO NS/graphene composite and the NiO NS−graphene mixture, which corresponds to the partial capacity contribution from the graphene. There are two plateaux located at about 1.25 and 2.25 V in the charge curves, which, respectively, originate from the

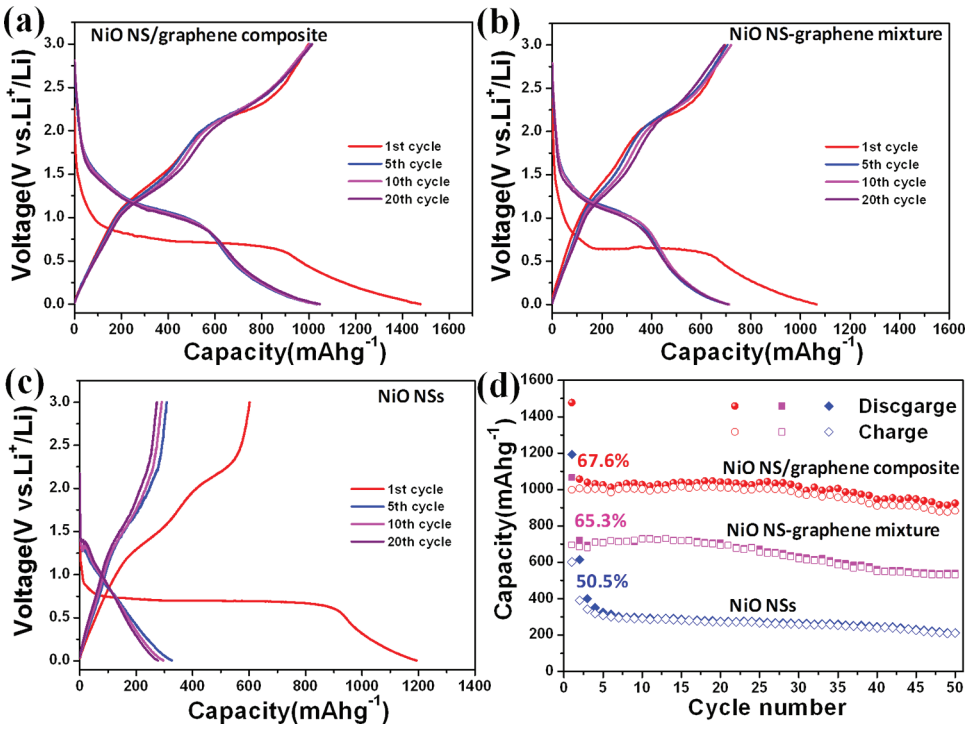

Figure 6. Galvanostatic charge–discharge profiles of the (a) NiO NS/graphene composite, (b) NiO NS–graphene mixture, and (c) NiO NSs. (d) Cycling performance and the first Coulombic efficiency of the NiO NS/graphene composite, NiO NS–graphene mixture, and NiO NSs at a current density of 50 mA g^{-1} for 50 cycles. Solid symbols, discharge; hollow symbols, charge.

decomposition of the SEI film and the reverse reaction for the formation of NiO from Ni and Li_2O.[25,48] In the subsequent discharge/charge process of the composite and mixture, the plateaux became higher and more sloping with a lower overpotential than those in the first cycle, indicating that the Li^+ insertion reaction is easier. On the contrary, the plateaux almost disappear, and the discharge potential decreases while the charge potential increases, exhibiting higher overpotential for NiO NSs. These results can be ascribed to the excellent electrical conductivity of graphene, the large contact area with the electrolyte, and the sheet-like nanostructure with a short diffusion pathway for lithium ions promoting the reaction kinetics of the composite. The cyclic voltammetry (CV) curves of the NiO NS/graphene composite and NiO NSs were tested over a voltage range from 0.001 to 3.0 V at a scan rate of 0.2 mV s^{-1}, showing a cathodic peak and two anodic peaks (Figure S9), and the peak intensity and integral areas of the NiO NS/graphene composite are close from the second cycle to the fifth, showing good cycle stability, but obviously decrease for the NiO NS electrode after the first cycle. These resuts are consistent with the galvanostatic charge–discharge measurements.

Figure 6d shows the cycling performance and the first Coulombic efficiency of the NiO NS/graphene composite, NiO NS–graphene mixture, and NiO NSs at a current density of 50 mA g^{-1}. The NiO NS/graphene composite exhibits a discharge capacity of 1478 mA h g^{-1} and a high initial reversible capacity

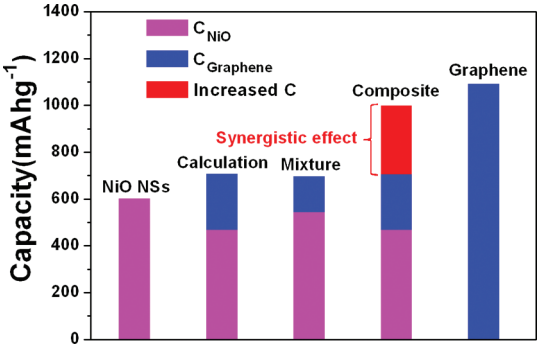

Figure 7. First reversible specific capacity of the graphene, NiO NSs, NiO NS/graphene composite, NiO NS–graphene mixture, and the calculated specific capacity based on experimental values. The red rectangle indicates the increased capacity due to the synergistic effect between graphene and NiO NSs.

(1000 mA h g^{-1}), obviously larger than the values for the NiO NS–graphene mixture (1066 and 696 mA h g^{-1}) and NiO NSs (1193 and 602 mA h g^{-1}). The first reversible capacity of the NiO NS–graphene mixture (696 mA h g^{-1}) approaches the theoretical value of the total sum ($602 \times 78.2\% + 1091 \times 21.8\% = 709$ mA h g^{-1}) of the individual capacities of NiO NSs (602 mA h g^{-1}) and graphene (1091 mA h g^{-1}, Figure S10), suggesting a simple principle of superposition between graphene and NiO NSs (Figure 7). However, the capacity of the NiO NS/graphene composite is much higher than the total sum of the individual capacities of NiO NSs and graphene, indicating a synergistic effect between

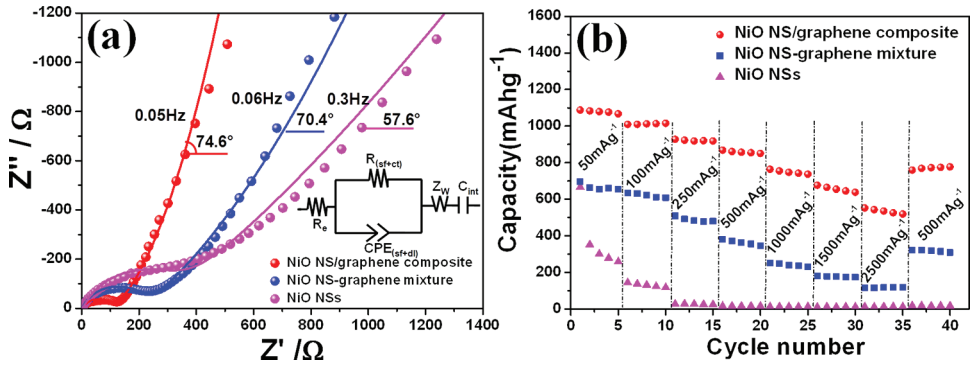

Figure 8. (a) Nyquist plots of the NiO NS/graphene composite, NiO NS−graphene mixture, and NiO NSs as anode materials measured after the first cycle at a current density of 250 mA g^{-1} in the charged state (3.0 V *vs* Li^+/Li) and the equivalent electrical circuit (inset) used to fit the experimental impedance spectra. Selected frequencies are shown. Symbols denote experimental data, while the continuous lines represent the fitted data. (b) Rate performance of the NiO NS/graphene composite, NiO NS−graphene mixture, and NiO NSs at different current densities.

these two components. The NiO NS/graphene composite shows a stable reversible capacity of 883 mA h g^{-1} after 50 charge/discharge cycles, corresponding to ~90% retention of the initial capacity, which is much better than that of the NiO NS−graphene mixture (530 mA h g^{-1}, 76% retention) and the NiO NSs (210 mA h g^{-1} and only 35% retention) (Figure 6d). The first Coulombic efficiency also significantly increases to 67.6% for the composite and remains steady at a value >96% after the first cycle, compared to the NiO NSs with a first Coulombic efficiency of 50.5% and slowly increasing Coulombic efficiency. This suggests that good binding in the composite in which graphene provides fast electron transport for NiO NSs and the porous characteristics of the composite with easy ion accessibility promoting the conversion reaction improve the efficiency. The flexible graphene provides good strain accommodation mitigating the volume change of NiO NSs during cycling, which helps improve the cycling stability.

The oxygen bridges between graphene and NiO NSs also contribute to the good conductivity of the composites, which directly correlates to the excellent electrochemical performance and is confirmed by electrochemical impedance spectroscopy (EIS) measurements. These cells were measured after the first cycle at a current density of 250 mA g^{-1} in the charged state (3.0 V *vs* Li^+/Li), as shown in Figure 8a. The Nyquist plots of the electrodes are constituted by a single depressed semicircle in the high-medium frequency region and an inclined line at low frequency. The experimental data are represented as symbols, and the continuous lines are fitted data according to the equivalent circuit shown in the inset of Figure 8a.[7,49−51] The elements in the equivalent circuit include ohmic resistance of the electrolyte and cell components (R_e), surface film resistance (R_{sf}), charge-transfer resistance at the interface between the electrode and electrolyte (R_{ct}), a constant phase element (CPE_i) (sf, double layer (dl)) used instead of pure capacitance due to the depressed semicircle, Warburg impedance (Z_w), and intercalation capacitance (C_{int}).[49,50] According to the fitting, the value of R_e is 1.3−1.9 Ω for the three samples, indicating that the cells have been properly fabricated and tested in the same condition. Due to the single semicircle observed, the impedance can be ascribed to the combination of the surface film and charge-transfer resistance $R_{(sf+ct)}$.[49,50] The fitting parameter of $R_{(sf+ct)}$ is much lower for the NiO NS/graphene composite electrode (105.6 Ω) compared to the NiO NS−graphene mixture (213.3 Ω) and NiO NS electrode (279.9 Ω), which means that the NiO NS/graphene composite electrode has a more stable surface film (including SEI layer) and faster charge-transfer process than the others. It can be seen that the low-frequency tail for the three samples was also different, which can be compared qualitatively with reference to the mass (mainly of lithium ions) transfer kinetics in the electrode materials. The low-frequency slope angle is 74.6° for the NiO NS/graphene composite electrode, higher than that of NiO NS−graphene mixture (70.4°) and NiO NS electrode (57.6°). The steeper low-frequency tail indicates higher lithium ion conductivity in the electrode materials.[52] As expected, it indicates that the NiO NS/graphene composite electrode possesses a high electrical conductivity, a rapid charge-transfer process, and good Li-ion kinetics for lithium uptake and extraction. Therefore, the NiO NS/graphene composite exhibits outstanding high-rate performance compared to the NiO NS−graphene mixture and NiO NSs, as shown in Figure 8b. The composite and mixture deliver a stable specific capacity above 1000 and 680 mA h g^{-1}, respectively, for five cycles under a current density of 50 mA g^{-1}. On the other hand, the NiO NSs retain only 39% of the first charge capacity at the fifth cycle under the same test conditions. With increasing current density, the superior rate capacity of the NiO NS/graphene composite is more evident. When the discharge and charge current density increase to as high as 2.5 A g^{-1}, the specific capacity of the composite

remains at 550 mA h g^{-1}, which is highly attractive compared with other high-performance nanostructured NiO-based anode materials.[18,25,32,53,54] However, the capacity of the NiO NS–graphene mixture drops dramatically to about 100 mA h g^{-1} at the same current density, and the NiO NS electrode becomes unusable with cycling only at a low current density of 0.25 A g^{-1}. Moreover, when the current rate is returned to the value of 0.5 A g^{-1}, the composite electrode resumes its capacity of about 775 mA h g^{-1} after 35 cycles at various current densities, indicating that the NiO NS/graphene composite electrode has good rate capability and cycling stability. The excellent rate performance of the NiO NS/graphene composite can be attributed to the good binding between the two components, favorable charge-transport characteristics of the combination of graphene with the 2D nanosheet structure of NiO, together with the short diffusion length of lithium ions in the thickness direction.

The attractive electrochemical performance of the NiO NS/graphene composite demonstrated above could be attributed to the oxygen bridges between graphene and NiO NSs, inducing a synergistic effect from the two components. The unique sheet-on-sheet nanostructure prevents the restacking of graphene, which improves the utilization of active material. The NiO NSs grown directly on the graphene have good adhesion and electrical contact with the graphene. This is confirmed by the SEM image after 50 cycles (Figure S11a) and TEM image after discharge (Figure S11c) in which NiO NSs are still closely anchored to the graphene compared to the agglomerated bare NiO NSs (Figure S11b,d). The graphene increases the electrical conductivity of the electrode and is able to accommodate the strain induced by volume change of NiO NSs. It also maintains the integrity of the electrode during discharge–charge, which is responsible for the good cycling stability and rate capability.

CONCLUSIONS

NiO NSs were directly grown on graphene to fabricate a multilayer structure, in which oxygen bridges were formed between graphene and NiO NSs, producing a synergistic effect to improve the lithium storage behavior of the composite. The highly improved performance of the NiO NS/graphene composite can be understood by the pinning effect of hydroxyl/epoxy groups on the Ni atoms of NiO NSs based on first-principles calculations. The experimental and calculated results for the oxygen bridges between graphene and NiO NSs will help us in designing and obtaining high-performance electrode materials. The binding through oxygen bridges demonstrated in this work could be extended to other metal oxide/graphene composites for applications in many fields such as energy storage, catalysis, sensing, electrocatalysis, and optoelectronics for pursuing optimal performance.

EXPERIMENTAL SECTION

Synthesis of Graphene. Graphene was prepared from natural flake graphite powder by chemical exfoliation as reported in our previous work.[55]

Synthesis of NiO NS/Graphene Composite. First, 50 mg graphene was dispersed in 50 mL of an isopropyl alcohol–water (1:1, v/v) solution with 0.03 M $Ni(NO_3)_2$ by sonication for 1 h. Then, an appropriate amount of ammonia solution ($NH_3 \cdot H_2O$, 25 wt %) was slowly added to this suspension and stirred for 2 h. The mixed suspension was sealed in an 80 mL Teflon-lined stainless steel autoclave for hydrothermal reaction at 180 °C for 6 h. The product was collected after centrifuging, washing with deionized water followed by alcohol, and then drying at 80 °C in air for 12 h. Finally, the samples were heated to 350 °C with a ramp of 5 °C min^{-1}, where they were annealed for 3 h under an argon atmosphere to obtain the NiO NS/graphene composite.

Synthesis of Pure NiO NSs. The synthesis procedure was the same as that for the NiO NS/graphene composite but without adding graphene.

Synthesis of NiO NS–Graphene Mixture. The mixture was prepared by adding the same amount of graphene and NiO NSs as that in the NiO NS/graphene composite through grinding in a mortar at room temperature for 0.5 h.

Materials Characterization. The morphology, composition, and structure of the samples were characterized by TEM (Tecnai F20, 200 kV), SEM (FEI Nova NanoSEM 430, 15 kV), micro-Raman spectroscopy (Jobin Yvon LabRam HR800, excited by 632.8 nm He–Ne laser), and TGA (Netzsch-STA 449C, measured from 30 to 800 °C at a heating rate of 10 °C min^{-1} in air). XPS analysis was performed on an ESCALAB 250 instrument with Al Kα radiation (15 kV, 150 W) under a pressure of 4×10^{-8} Pa. N_2 adsorption–desorption isotherms were determined by a Micromeritics ASAP 2020M. FTIR spectra were obtained using a Bruker TENSOR 27 spectrometer. The samples were collected using the KBr pellet method, and the obtained spectra were normalized using OPUS 6.5 software.

Electrochemical Measurements. The electrochemical properties of the NiO NS/graphene composite, NiO NS–graphene mixture, graphene, and NiO NSs as anode materials in half cells were evaluated by a galvanostatic charge/discharge technique. The test electrodes were prepared by mixing 80 wt % active material with 10 wt % conductive carbon black (super P) as a conducting agent and 10 wt % polyvinylidene fluoride dissolved in *N*-methyl-2-pyrrolidone as a binder to form a slurry, which was then coated onto a copper foil and dried under vacuum at 120 °C for 12 h. The foil was pressed between twin rollers, shaped into a circular pellet with a diameter of 12 mm and finally dried in a vacuum oven at 120 °C for 6 h. The active material in the electrode was about 1–2 mg, and the geometrical area of the electrode was 1.13 cm^2. Coin cells (size 2032) were assembled in an argon-filled glovebox with the samples as test electrode, metallic lithium as the counter/reference electrode, a mixture of 1 M $LiPF_6$ in ethylene carbonate, dimethyl carbonate, and ethylmethyl carbonate (1:1:1 vol) as the electrolyte, and Celgard 2400 polypropylene as the separator. Charge–discharge measurements were carried out galvanostatically at various current densities over a voltage range of 0.001 to 3 V (*vs* Li/Li^+) using a battery testing system (LAND CT2001A). After 50 cycles or the first discharge, the cells were disassembled in the glovebox, and the working electrode was taken out and washed three times using a dimethyl carbonate solution. It was then transferred using a sealed container into the vacuum chamber of the SEM/TEM for structure characterization. CV measurements were carried out using a Solartron 1287 electrochemical

workstation in the voltage range of 0.001−3.0 V (*vs* Li^+/Li) at a scan rate of 0.2 mV s^{-1}. EIS measurements were carried out by applying a perturbation voltage of 10 mV in a frequency range of 100 kHz to 10 mHz using a Solartron 1287/1260 electrochemical workstation.

First-Principles Calculations. Total energy calculations were carried out by using DFT implemented in the Vienna ab initio simulation package,[56] using the generalized gradient approximation of Perdew−Burke−Ernzerhof.[57] The electron−ion interactions were described by the projector-augmented wave approach.[58,59] The energy cutoff for the plane wave expansion was set to 544 eV to ensure sufficient convergence (less than 1 meV/cell). A large 2D (4 × 4) supercell consisting of 32 C atoms was constructed to represent the graphene, as shown in Figure S7a. In the case of HO-graphene, a 2D periodic supercell including 56 atoms (40 C atoms and 8 hydroxyl groups) was built (see Figure S7b), and a 2D supercell including 40 C atoms and 4 epoxy groups was constructed to simulate the structure of EO-graphene (see Figure S8), in which the hydroxyl/epoxy groups form a stable armchair chain on both sides of the graphene by polymerizing.[60] The vacuum space in the *z* direction was set to be 20 Å, thus the *k*-space sampling was restricted to the Γ-point for all calculations. All atomic positions were relaxed to an energy convergence of 10^{-4} eV (equating to a force convergence of 10^{-2} eV/Å). To investigate the diffusion dynamics for an isolated Ni adatom on the surface of a graphene and the detachment process of a bonded Ni on the HO-graphene/EO-graphene, we calculated the corresponding energy barriers by using the cNEB method.[61−63]

Conflict of Interest: The authors declare no competing financial interest.

Acknowledgment. This work was supported by National Science Foundation of China (Nos. 50921004 and 51172239) and Chinese Academy of Sciences. We acknowledge the grant from the GPU project of MOF (No. ZDYZ2008-2-A12) and support from the Informalization Construction Project (No. INFO-115-B01) and the Supercomputing Center, CAS, China. We thank J. H. Luo for FTIR support.

Supporting Information Available: Figures S1−S11. This material is available free of charge *via* the Internet at http://pubs.acs.org.

REFERENCES AND NOTES

1. Poizot, P.; Laruelle, S.; Grugeon, S.; Dupont, L.; Tarascon, J. M. Nano-Sized Transition-Metal Oxides as Negative-Electrode Materials for Lithium-Ion Batteries. *Nature* **2000**, *407*, 496–499.
2. Tarascon, J. M.; Armand, M. Issues and Challenges Facing Rechargeable Lithium Batteries. *Nature* **2001**, *414*, 359–367.
3. Arico, A. S.; Bruce, P.; Scrosati, B.; Tarascon, J. M.; Van Schalkwijk, W. Nanostructured Materials for Advanced Energy Conversion and Storage Devices. *Nat. Mater.* **2005**, *4*, 366–377.
4. Guo, Y. G.; Hu, J. S.; Wan, L. J. Nanostructured Materials for Electrochemical Energy Conversion and Storage Devices. *Adv. Mater.* **2008**, *20*, 2878–2887.
5. Liu, C.; Li, F.; Ma, L.-P.; Cheng, H.-M. Advanced Materials for Energy Storage. *Adv. Mater.* **2010**, *22*, E28–E62.
6. Kim, M. G.; Cho, J. Reversible and High-Capacity Nanostructured Electrode Materials for Li-Ion Batteries. *Adv. Funct. Mater.* **2009**, *19*, 1497–1514.
7. Reddy, M. V.; Rao, G. V. S.; Chowdari, B. V. R. Nano-$(V_{1/2}Sb_{1/2}Sn)O_4$: A High Capacity, High Rate Anode Material for Li-Ion Batteries. *J. Mater.Chem.* **2011**, *21*, 10003–10011.
8. Reddy, M. V.; Beichen, Z.; Nicholette, L. J.; Kaimeng, Z.; Chowdari, B. V. R. Molten Salt Synthesis and Its Electrochemical Characterization of Co_3O_4 for Lithium Batteries. *Electrochem. Solid State Lett.* **2011**, *14*, A79–A82.
9. Pumera, M. Graphene-Based Nanomaterials and Their Electrochemistry. *Chem. Soc. Rev.* **2010**, *39*, 4146–4157.
10. Paek, S. M.; Yoo, E.; Honma, I. Enhanced Cyclic Performance and Lithium Storage Capacity of SnO_2/Graphene Nanoporous Electrodes with Three-Dimensionally Delaminated Flexible Structure. *Nano Lett.* **2009**, *9*, 72–75.
11. Zhu, Y. W.; Murali, S.; Cai, W. W.; Li, X. S.; Suk, J. W.; Potts, J. R. Ruoff, R. S. Graphene and Graphene Oxide: Synthesis, Properties, and Applications. *Adv. Mater.* **2010**, *22*, 3906–3924.
12. Zhou, G. M.; Wang, D. W.; Li, F.; Zhang, L. L.; Li, N.; Wu, Z. S.; Wen, L.; Lu, G. Q.; Cheng, H. M. Graphene-Wrapped Fe_3O_4 Anode Material with Improved Reversible Capacity and Cyclic Stability for Lithium Ion Batteries. *Chem. Mater.* **2010**, *22*, 5306–5313.
13. Wu, Z. S.; Ren, W. C.; Wen, L.; Gao, L. B.; Zhao, J. P.; Chen, Z. P.; Zhou, G. M.; Li, F.; Cheng, H. M. Graphene Anchored with Co_3O_4 Nanoparticles as Anode of Lithium Ion Batteries with Enhanced Reversible Capacity and Cyclic Performance. *ACS Nano* **2010**, *4*, 3187–3194.
14. Yang, S. B.; Feng, X. L.; Ivanovici, S.; Mullen, K. Fabrication of Graphene-Encapsulated Oxide Nanoparticles: Towards High-Performance Anode Materials for Lithium Storage. *Angew. Chem., Int. Ed.* **2010**, *49*, 8408–8411.
15. Wang, D.; Kou, R.; Choi, D.; Yang, Z.; Nie, Z.; Li, J.; Saraf, L. V.; Hu, D.; Zhang, J.; Graff, G. L.; *et al.* Ternary Self-Assembly of Ordered Metal Oxide−Graphene Nanocomposites for Electrochemical Energy Storage. *ACS Nano* **2010**, *4*, 1587–1595.
16. Yao, J.; Shen, X. P.; Wang, B.; Liu, H. K.; Wang, G. X. *In Situ* Chemical Synthesis of SnO_2-Graphene Nanocomposite as Anode Materials for Lithium-Ion Batteries. *Electrochem. Commun.* **2009**, *11*, 1849–1852.
17. Wang, H.; Cui, L.-F.; Yang, Y.; Sanchez Casalongue, H.; Robinson, J. T.; Liang, Y.; Cui, Y.; Dai, H. Mn_3O_4−Graphene Hybrid as a High-Capacity Anode Material for Lithium Ion Batteries. *J. Am. Chem. Soc.* **2010**, *132*, 13978–13980.
18. Zou, Y. Q.; Wang, Y. NiO Nanosheets Grown on Graphene Nanosheets as Superior Anode Materials for Li-Ion Batteries. *Nanoscale* **2011**, *3*, 2615–2620.
19. Wang, H. L.; Casalongue, H. S.; Liang, Y. Y.; Dai, H. J. $Ni(OH)_2$ Nanoplates Grown on Graphene as Advanced Electrochemical Pseudocapacitor Materials. *J. Am. Chem. Soc.* **2010**, *132*, 7472–7477.
20. Wu, Z. S.; Wang, D. W.; Ren, W.; Zhao, J.; Zhou, G. M.; Li, F.; Cheng, H. M. Anchoring Hydrous RuO_2 on Graphene Sheets for High-Performance Electrochemical Capacitors. *Adv. Funct. Mater.* **2010**, *20*, 3595–3602.
21. Wang, H.; Robinson, J. T.; Diankov, G.; Dai, H. Nanocrystal Growth on Graphene with Various Degrees of Oxidation. *J. Am. Chem. Soc.* **2010**, *132*, 3270–3271.
22. Lightcap, I. V.; Kosel, T. H.; Kamat, P. V. Anchoring Semiconductor and Metal Nanoparticles on a Two-Dimensional Catalyst Mat. Storing and Shuttling Electrons with Reduced Graphene Oxide. *Nano Lett.* **2010**, *10*, 577–583.
23. Wu, Z.-S.; Zhou, G. M.; Yin, L.-C.; Ren, W.; Li, F.; Cheng, H.-M. Graphene/Metal Oxide Composite Electrode Materials for Energy Storage. *Nano Energy* **2012**, *1*, 107–131.
24. Ding, S.; Luan, D.; Boey, F. Y. C.; Chen, J. S.; Lou, X. W. SnO_2 Nanosheets Grown on Graphene Sheets with Enhanced Lithium Storage Properties. *Chem. Commun.* **2011**, *47*, 7155–7157.
25. Varghese, B.; Reddy, M. V.; Yanwu, Z.; Lit, C. S.; Hoong, T. C.; Rao, G. V. S.; Chowdari, B. V. R.; Wee, A. T. S.; Lim, C. T.; Sow, C. H. Fabrication of NiO Nanowall Electrodes for High Performance Lithium Ion Battery. *Chem. Mater.* **2008**, *20*, 3360–3367.
26. Hu, J.; Ramadan, A.; Luo, F.; Qi, B.; Deng, X.; Chen, J. One-Step Molybdate Ion Assisted Electrochemical Synthesis of α-MoO_3-Decorated Graphene Sheets and Its Potential Applications. *J. Mater. Chem.* **2011**, *21*, 15009–15014.
27. Liu, L.; Li, Y.; Yuan, S. M.; Ge, M.; Ren, M. M.; Sun, C. S.; Zhou, Z. Nanosheet-Based NiO Microspheres: Controlled Solvothermal Synthesis and Lithium Storage Performances. *J. Phys. Chem. C* **2010**, *114*, 251–255.
28. Lv, W.; Tang, D. M.; He, Y. B.; You, C. H.; Shi, Z. Q.; Chen, X. C.; Chen, C. M.; Hou, P. X.; Liu, C.; Yang, Q. H. Low-Temperature Exfoliated Graphenes: Vacuum-Promoted Exfoliation and Electrochemical Energy Storage. *ACS Nano* **2009**, *3*, 3730–3736.

29. Gardner, S. D.; Singamsetty, C. S. K.; Booth, G. L.; He, G. R.; Pittman, C. U. Surface Characterization of Carbon-Fibers Using Angle-Resolved XPS and ISS. *Carbon* **1995**, *33*, 587–595.
30. Pei, S.; Zhao, J.; Du, J.; Ren, W.; Cheng, H.-M. Direct Reduction of Graphene Oxide Films into Highly Conductive and Flexible Graphene Films by Hydrohalic Acids. *Carbon* **2010**, *48*, 4466–4474.
31. Goto, Y.; Taniguchi, K.; Omata, T.; Otsuka-Yao-Matsuo, S.; Ohashi, N.; Ueda, S.; Yoshikawa, H.; Yamashita, Y.; Oohashi, H.; Kobayashi, K. Formation of Ni_3C Nanocrystals by Thermolysis of Nickel Acetylacetonate in Oleylamine: Characterization Using Hard X-ray Photoelectron Spectroscopy. *Chem. Mater.* **2008**, *20*, 4156–4160.
32. Kottegoda, I. R. M.; Idris, N. H.; Lu, L.; Wang, J. Z.; Liu, H. K. Synthesis and Characterization of Graphene-Nickel Oxide Nanostructures for Fast Charge-Discharge Application. *Electrochim. Acta* **2011**, *56*, 5815–5822.
33. Park, S.; Lee, K. S.; Bozoklu, G.; Cai, W.; Nguyen, S. T.; Ruoff, R. S. Graphene Oxide Papers Modified by Divalent Ions—Enhancing Mechanical Properties *via* Chemical Cross-Linking. *ACS Nano* **2008**, *2*, 572–578.
34. Xia, X. H.; Tu, J. P.; Zhang, J.; Wang, X. L.; Zhang, W. K.; Huang, H. Electrochromic Properties of Porous NiO Thin Films Prepared by a Chemical Bath Deposition. *Sol. Energy Mater. Sol. Cells* **2008**, *92*, 628–633.
35. Park, S.; An, J. H.; Jung, I. W.; Piner, R. D.; An, S. J.; Li, X. S.; Velamakanni, A.; Ruoff, R. S. Colloidal Suspensions of Highly Reduced Graphene Oxide in a Wide Variety of Organic Solvents. *Nano Lett.* **2009**, *9*, 1593–1597.
36. Stankovich, S.; Piner, R. D.; Nguyen, S. T.; Ruoff, R. S. Synthesis and Exfoliation of Isocyanate-Treated Graphene Oxide Nanoplatelets. *Carbon* **2006**, *44*, 3342–3347.
37. Ferrari, A. C.; Robertson, J. Interpretation of Raman Spectra of Disordered and Amorphous Carbon. *Phys. Rev. B* **2000**, *61*, 14095–14107.
38. Rao, A. M.; Eklund, P. C.; Bandow, S.; Thess, A.; Smalley, R. E. Evidence for Charge Transfer in Doped Carbon Nanotube Bundles from Raman Scattering. *Nature* **1997**, *388*, 257–259.
39. Kitaura, R.; Imazu, N.; Kobayashi, K.; Shinohara, H. Fabrication of Metal Nanowires in Carbon Nanotubes *via* Versatile Nano-Template Reaction. *Nano Lett.* **2008**, *8*, 693–699.
40. Zhou, J. S.; Song, H. H.; Ma, L. L.; Chen, X. H. Magnetite/Graphene Nanosheet Composites: Interfacial Interaction and Its Impact on the Durable High-Rate Performance in Lithium-Ion Batteries. *RSC Adv.* **2011**, *1*, 782–791.
41. Wang, W. Z.; Liu, Y. K.; Xu, C. K.; Zheng, C. L.; Wang, G. H. Synthesis of NiO Nanorods by a Novel Simple Precursor Thermal Decomposition Approach. *Chem. Phys. Lett.* **2002**, *362*, 119–122.
42. Bagri, A.; Mattevi, C.; Acik, M.; Chabal, Y. J.; Chhowalla, M.; Shenoy, V. B. Structural Evolution During the Reduction of Chemically Derived Graphene Oxide. *Nat. Chem.* **2010**, *2*, 581–587.
43. Kittel, C. *Introduction to Solid State Physics*; Wiley: New York, 2005; p 50.
44. Johll, H.; Kang, H. C.; Tok, E. S. Density Functional Theory Study of Fe, Co, and Ni Adatoms and Dimers Adsorbed on Graphene. *Phys. Rev. B* **2009**, *79*, 245416.
45. Cao, C.; Wu, M.; Jiang, J.; Cheng, H.-P. Transition Metal Adatom and Dimer Adsorbed on Graphene: Induced Magnetization and Electronic Structures. *Phys. Rev. B* **2010**, *81*, 205424.
46. Hu, L.; Hu, X.; Wu, X.; Du, C.; Dai, Y.; Deng, J. Density Functional Calculation of Transition Metal Adatom Adsorption on Graphene. *Phys. B* **2010**, *405*, 3337–3341.
47. Hamaed, A.; Trudeau, M.; Antonelli, D. M. H_2 Storage Materials (22 kJ/mol) Using Organometallic Ti Fragments as Σ-H_2 Binding Sites. *J. Am. Chem. Soc.* **2008**, *130*, 6992–6999.
48. Huang, X. H.; Tu, J. P.; Zhang, B.; Zhang, C. Q.; Li, Y.; Yuan, Y. F.; Wu, H. M. Electrochemical Properties of NiO-Ni Nanocomposite as Anode Material for Lithium Ion Batteries. *J. Power Sources* **2006**, *161*, 541–544.
49. Reddy, M. V.; Yu, T.; Sow, C. H.; Shen, Z. X.; Lim, C. T.; Rao, G. V. S.; Chowdari, B. V. R. α-Fe_2O_3 Nanoflakes as an Anode Material for Li-Ion Batteries. *Adv. Funct. Mater.* **2007**, *17*, 2792–2799.
50. Reddy, M. V.; Madhavi, S.; Subba Rao, G. V.; Chowdari, B. V. R. Metal Oxyfluorides $TiOF_2$ and NbO_2F as Anodes for Li-Ion Batteries. *J. Power Sources* **2006**, *162*, 1312–1321.
51. Sakunthala, A.; Reddy, M. V.; Selvasekarapandian, S.; Chowdari, B. V. R.; Selvin, P. C. Preparation, Characterization, and Electrochemical Performance of Lithium Trivanadate Rods by a Surfactant-Assisted Polymer Precursor Method for Lithium Batteries. *J. Phys. Chem. C* **2010**, *114*, 8099–8107.
52. Ma, Y.; Zhang, C.; Ji, G.; Lee, J. Y. Nitrogen-Doped Carbon-Encapsulation of Fe_3O_4 for Increased Reversibility in Li^+ Storage by the Conversion Reaction. *J. Mater.Chem.* **2012**, DOI: 10.1039/C2JM30422H.
53. Wang, X. H.; Li, X. W.; Sun, X. L.; Li, F.; Liu, Q. M.; Wang, Q.; He, D. Y. Nanostructured NiO Electrode for High Rate Li-Ion Batteries. *J. Mater.Chem.* **2011**, *21*, 3571–3573.
54. Cheng, M. Y.; Hwang, B. J. Mesoporous Carbon-Encapsulated NiO Nanocomposite Negative Electrode Materials for High-Rate Li-Ion Battery. *J. Power Sources* **2010**, *195*, 4977–4983.
55. Wu, Z. S.; Ren, W. C.; Gao, L. B.; Liu, B. L.; Jiang, C. B.; Cheng, H. M. Synthesis of High-Quality Graphene with a Predetermined Number of Layers. *Carbon* **2009**, *47*, 493–499.
56. Kresse, G.; Furthmuller, J. Efficient Iterative Schemes for *Ab Initio* Total-Energy Calculations Using a Plane-Wave Basis Set. *Phys. Rev. B* **1996**, *54*, 11169–11186.
57. Perdew, J. P.; Burke, K.; Ernzerhof, M. Generalized Gradient Approximation Made Simple. *Phys. Rev. Lett.* **1996**, *77*, 3865–3868.
58. Blochl, P. E. Projector Augmented-Wave Method. *Phys. Rev. B* **1994**, *50*, 17953–17979.
59. Kresse, G.; Joubert, D. From Ultrasoft Pseudopotentials to the Projector Augmented-Wave Method. *Phys. Rev. B* **1999**, *59*, 1758–1775.
60. Wang, L.; Sun, Y. Y.; Lee, K.; West, D.; Chen, Z. F.; Zhao, J. J.; Zhang, S. B. Stability of Graphene Oxide Phases from First-Principles Calculations. *Phys. Rev. B* **2010**, *82*, 161406.
61. Sheppard, D.; Terrell, R.; Henkelman, G. Optimization Methods for Finding Minimum Energy Paths. *J. Chem. Phys.* **2008**, *128*, 134106.
62. Henkelman, G.; Uberuaga, B. P.; Jonsson, H. A Climbing Image Nudged Elastic Band Method for Finding Saddle Points and Minimum Energy Paths. *J. Chem. Phys.* **2000**, *113*, 9901–9904.
63. Henkelman, G.; Jonsson, H. Improved Tangent Estimate in the Nudged Elastic Band Method for Finding Minimum Energy Paths and Saddle Points. *J. Chem. Phys.* **2000**, *113*, 9978–9985.